ACS APPLIED MATERIALS & INTERFACES

www.acsami.org

Research Article

Tuning the Ion-Selectivity of Thin-Film Composite Nanofiltration Membranes by Molecular Layer Deposition of Alucone

Sanhita Chaudhury, Eyal Wormser, Yuval Harari, Eran Edri,* and Oded Nir*

Cite This: *ACS Appl. Mater. Interfaces* 2020, 12, 53356–53364

Read Online

ACCESS | Metrics & More | Article Recommendations | Supporting Information

ABSTRACT: This work addresses a key challenge of tailoring the ion selectivity of a thin-film composite nanofiltration membrane to a specific application, such as water softening, without altering the water permeability. We modified the active surface of a commercial NF270 membrane by molecular layer deposition (MLD) of ethylene glycol-Al (EG-alucone). With increasing deposition cycles, we found that the MLD precursors first infiltrated and deposited in the active layer of NF270, then inflated the active layer, and finally deposited on the surface as a distinct EG-alucone layer. The deposition process changed the morphology of the membrane active layer and decreased the overall density of its fixed negative charge by embedding the positively charged EG-alucone. Filtration experiments revealed that these modifications affected the ion separation properties of the membrane without significantly hindering the water permeability. Specifically, the permeation of Na^+ increased relative to that of Mg^{2+}, as indicated by the permselectivity of Na^+ salts over Mg^{2+} salts. The changes in permselectivities with an increasing number of MLD cycles were rationalized using the dielectric, steric, and electrostatic ion exclusion mechanisms, which are related to the membrane material, pore size, and fixed charge, respectively. These relations open a path for the rational design of nanofiltration membranes with tailored selectivity by tuning the properties of the MLD layer. Filtration results of *natural brackish groundwater* using the MLD modified membranes agreed with the single salt experiments. As a result, water hardness was 26% lower for the permeate obtained using the MLD-modified membranes, which were found stable even during a 24 h filtration run. These results highlight the practical potential of this approach in enhancing water softening efficiency.

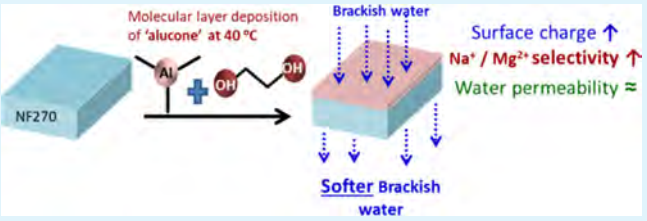

KEYWORDS: *ion selectivity, ion separation, membrane process, water treatment, filtration, atomic layer deposition*

1. INTRODUCTION

Ion-selective nanofiltration (NF) has potential use in applications such as wastewater reuse, industrial water treatment, water softening, and resource recovery.[1−4] Water softening—the removal of bivalent cations from water to avoid mineral precipitation—is heavily applied in many industries and has a projected global market value expected to exceed ten billion USD by 2024.[5] Currently, water softening is conducted mainly via induced chemical precipitation and ion exchange, both involving intensive chemical use.[6] NF, an economic, chemical-free, and low energy intensity membrane separation process, is a viable alternative technology for water softening because NF membrane properties can further be tailored to selectively permeate monovalent ions while retaining multivalent ones to the desired extent.[7,8] Researchers used polyelectrolyte multilayers,[9−12] graphene oxide/carbon nanotubes,[13,14] and copolymer micelles[15] to tune the selectivity of NF membranes. In most cases, the modification of the active layer added thickness or tightened the morphology of the membrane, adding resistance to water transport and reducing water permeability.[9] This trade-off[16,17] between ion-selectivity and water permeability impedes the development and practical implementation of ion-selective NF.[18] Alternatively, ion selectivity with minimal hindrance to water transport can be attained by minimizing the active layer thickness (while maintaining its uniformity), and by tuning the surface electrostatic charge type and density.

Metal oxides have a pH-dependent native surface charge in aqueous solution. Thin and uniform layers of metal oxides, hallmarks of layers deposited by atomic and molecular layer deposition (ALD, or MLD),[19−22] ensue these techniques promising routes to tailor membranes' surface properties to a specific application.[8,23−27] In comparison to ALD, MLD of organic−inorganic layers, such as alucones, has several potential advantages for coating membranes for water treatment: (1) the softer and more elastic nature of alucones have a better elastic matching with polymeric layers, which improves their stability;[28,29] (2) when soaked in water, alucone layers become porous with a sub-nm pore size that is

Received: September 14, 2020
Accepted: November 4, 2020
Published: November 16, 2020

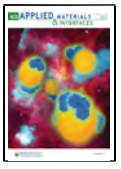

https://dx.doi.org/10.1021/acsami.0c16569
ACS Appl. Mater. Interfaces 2020, 12, 53356–53364

comparable to that of NF membranes.[30] As a result, alucone layers are not expected to tighten the membrane and hinder water transport. Yet, to date, we could find only three reports[31−33] on filtration membrane modification using MLD. In these publications,[31−33] a titanicone layer was deposited on the ceramic ultrafiltration membrane (pore size ∼ 30 nm) to transform it into a ceramic NF membrane (pore size 0.5−2 nm). An improvement in salt rejection and molecular weight cutoff was attained, showing the aptitude of this approach; however, the intercationic selectivity was not addressed.

In view of ion-selective NF for water softening, tuning the *surface* charge of the active layer is pivotal. In the current work, we used MLD to deposit aluminum-ethylene glycol (EG-alucone), a positively charged organic−inorganic layer, on a thin-film composite NF membrane (NF270), which is negatively charged.[9] We tested the applicability of the modified NF270 membranes to *real* brackish water softening. Additionally, we gained insight into the underlying ion selectivity mechanism by measuring the selectivity between Na^+ and Mg^{2+}-based salts,[10,13,34,35] and tested the stability of the membrane under continuous operation up to 24 h.

2. MATERIALS AND METHODS

The details of materials and chemicals are given in the Supporting Information and a brief description of the MLD of EG-alucone and the filtration process are given below.

2.1. MLD Process. The as-received NF270 membrane samples were directly subjected to MLD of EG-alucone in a GEMSstar XT benchtop ALD reactor chamber (Figure S1) at 40 °C. To maintain reproducibility, a similar area (5 × 10 cm^2) of the membrane was coated every time. Before starting the deposition, the membranes were kept in the chamber for 10 min under continuous 10 SCCM flow of Ar (99.999%). Each MLD cycle consisted of (1) 21 ms trimethylaluminium (TMA) pulse, (2) 60 s Ar purge, (3) 1000 ms EG pulse, and (4) 60 s Ar purge (Figure S2a, detailed in Supporting Information-section B). These steps were repeated for the desired number of cycles. Henceforth, the membranes are referred to in accordance with the number of MLD cycles used: "0 cycles" corresponds to the pristine NF270, and "X cycles" corresponds to the NF270 membrane modified with X MLD cycles. Postdeposition, the membranes were kept in water for at least three days to ensure complete conversion of the alucone to stable alumina.[19,30] The surface morphologies of the MLD-coated NF270 membranes were characterized using scanning electron microscopy (SEM using VERIOS XHR 460L, with samples coated by a ∼5 nm Ir layer) and atomic force microscopy (AFM), while the chemical changes due to MLD were monitored using attenuated total reflectance Fourier transform infrared spectroscopy (ATR−FTIR) and X-ray photoelectron spectroscopy (XPS). The zeta potentials and the water contact angles of these modified membranes were also measured. The details of all of these characterizations are given in the Supporting Information.

2.2. Filtration Experiments and Subsequent Analysis. The pure *water permeability* and the single salt ($MgSO_4$/Na_2SO_4/$MgCl_2$/NaCl) rejections were monitored using a crossflow filtration setup (Figure S14, further details in the Supporting Information) at 4 bar. Post MLD modification, the membranes were soaked in deionized water for 3 days and were compacted in the crossflow cell for 1 h at 3 bars before the filtration measurements. For all filtration experiments, the water flux through the membrane was determined according to the measured weight of the permeate (eq S1) and the *water permeability* of the membranes was determined from the pure water flux (eq S2). In the single-salt rejection experiments, the concentrations of the salts and the pH of the initial feed solution were 2 $g{\cdot}L^{-1}$ and 5.5 ± 0.1, respectively. Here, the observed rejection (R_o) of each salt was obtained from the measured electrical conductivities (using EUTECH conductivity meter-CON700) of the respective feed and permeate solutions (eq S3). Each measurement was repeated three times, each time with a new membrane and fresh salt solution.

The filtration performances of these membranes were also tested for a *real brackish water* feed (1 L, 4 bar) using the same filtration setup as described above. Before the filtration experiment, the as-received *brackish water* (Table S4, collected in Israel's southern district) was filtered using a Whatman filter paper and then the pH was adjusted (from original pH 6.9) to 5.8 using HCl. The R_o for each ion was determined from its measured concentrations (determined by inductively coupled plasma-atomic emission spectroscopy) in both feed and permeate (eq S4).

To decouple membrane transport phenomena from concentration polarization effects, the real salt passage, and the real rejection (R_r) were determined for each salt from R_o and the mass transfer coefficient (k) according to eq 1. For each salt "i", k_i was calculated from k_{MgSO_4}, which was estimated by an independent set of experiments as detailed in the Supporting Information (Section D2). The real (i.e., decoupled from concentration polarization) salt passage and real selectivity (α_j^i)[9,10] of sodium salt "i" over magnesium salt "j" were then obtained from eqs 1 and 2, respectively.

$$\text{Real salt passage } (\%) = 100 - \frac{C_p}{C_m} = 100 - R_r = 100 - \frac{100}{1 + e^{\left(\ln\left[\frac{1-R_0}{R_0}\right] - J_v/k\right)}} \quad (1)$$

$$\alpha_j^i = \frac{100 - R_r^i}{100 - R_r^j} \quad (2)$$

3. RESULTS AND DISCUSSION

3.1. Morphology of the MLD-Modified NF270 Active Layer. The surface of the pristine NF270 membrane, which contains a thin active piperazine-based semi-aromatic polyamide active layer (20−30 nm)[36] over a polysulfone support layer and a polyester-based fabric support,[37] changes significantly with progressive MLD cycles. Plan view SEM images after 5, 10, 25, 35, and 50 MLD cycles reveal that the pristine membrane surface is made of smooth granules (Figure 1a) that after 5 MLD cycles (Figure 1b) are mostly unchanged but appear coated with small nanometer-scale particles. At 10 MLD cycles (Figure 1c), large agglomerates with irregular shapes are apparent on top of the granulated surface, while a membrane coated with 25 MLD cycles has partly elongated and partly granulated regions (Figure 1d). The elongated features stem from interactions between the membrane substrate to the deposited layer or its components, as EG-alucone deposited (50 cycles) on a glass slide (hard substrate) had only spherical particles (Figure S6). At 35 MLD cycles (Figure 1e), the surface is mostly coated with elongated structures (width of 30−40 nm, and a length of 100−400 nm), and finally, at 50 cycles (Figure 1f), the elongated structures appear shorter, more irregular shaped, and more densely packed than at 35 cycles. Similar structural features appear in the AFM topography scans of the hydrated membranes (Figure S5) and confirm that the changes are not a result of drying (during SEM) the membrane. A detailed account of the topographic AFM analysis is given in the Supporting Information (Section C3).

Cross-section SEM images show that after 25 cycles of MLD, the active layer of the membrane becomes smooth and thicker (Figure 2C−E) than the pristine one (Figure 2A,B). This inflation indicates that the EG-alucone precursors infiltrate and deposit inside the active layer. The SEM images

https://dx.doi.org/10.1021/acsami.0c16569
ACS Appl. Mater. Interfaces 2020, 12, 53356−53364

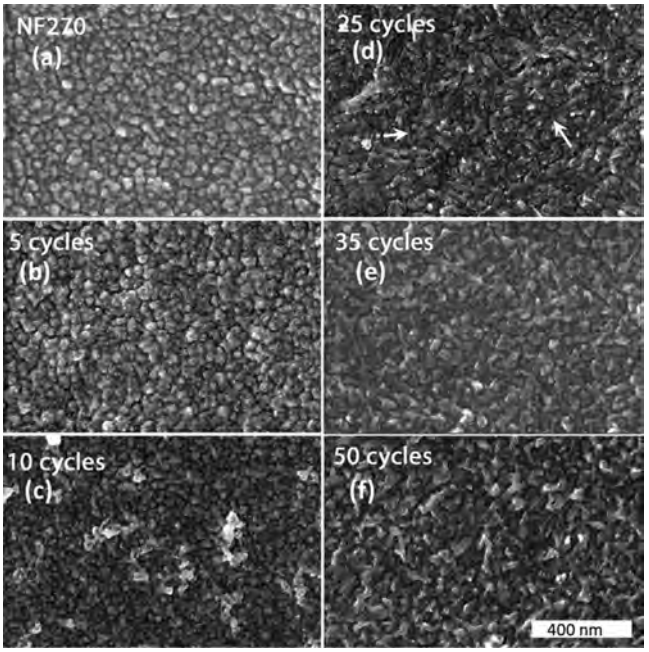

Figure 1. SEM images of the NF270 membrane surface with a sequential increase in coating cycles of EG-alucone. (a) Pristine NF270 membrane exhibit a granular surface texture, with a smooth granule surface. (b) After 5 cycles of MLD, the granules become rougher and small spots of a few nanometer scale can be seen uniformly throughout the surface. (c) Larger nucleation spots can be seen after 10 cycles, alongside the granulated membrane surface. (d) After 25 cycles, elongated shapes (polysulfone threads, marked by bold white arrows) appear along with spherical particles and the granulated membrane underneath. (e) After 35 cycles of MLD, the granulated surface of the NF270 is not apparent, rather the surface seems uniformly coated EG-alucone structures, both elongated and isotropic. (f) At 50 cycles, the surface is coated with densely packed elongated particles. Prior to imaging, the membranes were placed in water for at least three days, dried (at room temperature, no vacuum) and coated with Ir. Only contrast and brightness were modified in the images (using Adobe Photoshop CS6).

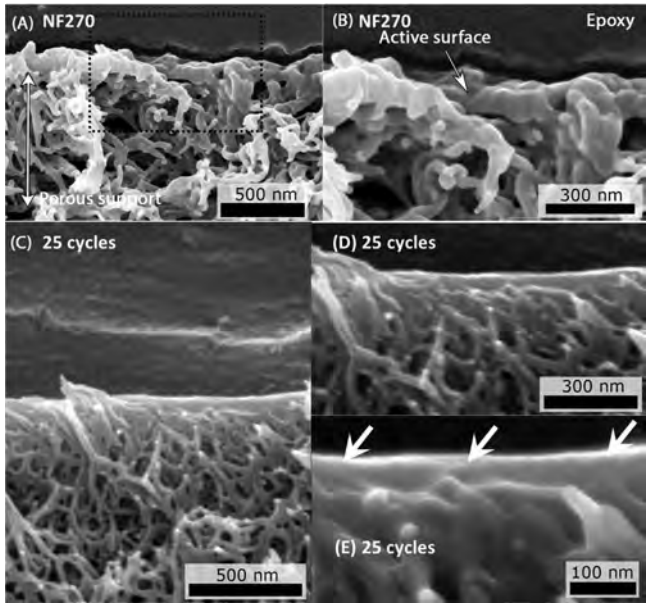

Figure 2. Cross-sectional SEM images of pristine and coated membranes. (A) Uncoated NF270—the polymeric threads of the porous polysulfone support layer are seen. The threads have a cross-section diameter of 30−50 nm. (B) Magnified region of the area bracketed in (A), showing the continuous active layer on top of the porous support. (C) NF270 coated with 25 cycles of EG-alucone. The porous support is seen together with a dense layer at the top of the membrane. (D) Magnified image of the bracketed region in (C) showing the dense layer is 100−200 nm thick. (E) Magnified image of the dense layer in (D) showing threads (bold white arrows) are intertwined with the dense layer at the top of the membrane. Prior to imaging, the membranes were placed in water for at least three days and dried. The dried samples were fixed to a glass substrate (using epoxy) with the active layer facing the glass, the glass slide was broken and the sections produced were coated with Ir and subjected to SEM imaging. The cross-sectional SEM images of the 5 and 50 MLD cycles modified NF270 membranes are shown in Figure S4.

(Figure 2C−E) also show that threads from the supporting layer become intertwined within the modified active layer, which suggests that the elongated shapes observed in hydrated AFM and plan view SEM are threads of the polysulfone support, exposed because of the MLD process. This hypothesis is supported by XPS measurements, as well as filtration results detailed in the sections below.

3.2. Composition of the MLD-Modified NF270 Active Layer. During the MLD process, the TMA can react with several probable active sites: (i) amides of NF270; (ii) carboxylic groups;[37] (iii) hydroxyl groups of EG. The reactions occur in parallel, but the dominance of each reaction varies as the MLD progress, as described herein. The Al to S (present in the polysulfone support) ratio increases linearly with increased MLD cycles (measured by EDS; Figure S7), while the S concentration within the electron beam excited depth (which is a few μm) is roughly constant, indicating a linear growth in Al content with progressive MLD cycles as expected. However, unlike in standard alucone MLD reactions, where both Al and O content increase jointly, on NF270 membranes, the surface concentration of O reduced after 5 MLD cycles, and only then gradually increased with further MLD cycles (surface concentration within the top ∼10 nm was measured by XPS; Supporting Information, Section C6, Figures S10c). This possibly indicates that in the several initial MLD cycles, a reaction (or reactions) of the precursors with the membranes' functional groups is more dominant than a reaction between TMA and EG. Last, as MLD progresses, the S 2p XPS spectrum reveals an increase in the S surface concentration (Figure S10b), with a second peak appearing at binding energy ∼172−173 eV (Figure S10a). We assign these peaks to the polysulfone support layer and the growth in S concentration to the changes in the membrane morphology, which exposes polysulfone threads to the X-ray beam as the MLD progresses. This assignment aligns with our SEM and AFM observations discussed above.

The variances in the FTIR spectra (Figure 3a,b; the penetration depth of an evanescent wave with a wavenumber of 3000 cm^{-1} into the membrane at the Ge/membrane interface is ∼150 nm) of MLD-modified NF270 with respect to pristine NF270 suggests that in the first 5 MLD cycles, TMA reacts with functional groups of the active layer and that EG deposits in the active layer. We observed a gradual decrease in the 2600−3600 cm^{-1} peaks intensity with increased MLD cycles but mostly in the higher wavenumber region that is associated with N−H bonds; an increase (Figure 3b) in the $\delta_s(CH_3)$ overtone (2700 cm^{-1}), which is commonly observed in the deposition of EG-alucone using TMA; and an increase in $-CH_2$ stretching bands (2852 and 2923 cm^{-1}), which we

https://dx.doi.org/10.1021/acsami.0c16569
ACS Appl. Mater. Interfaces 2020, 12, 53356−53364

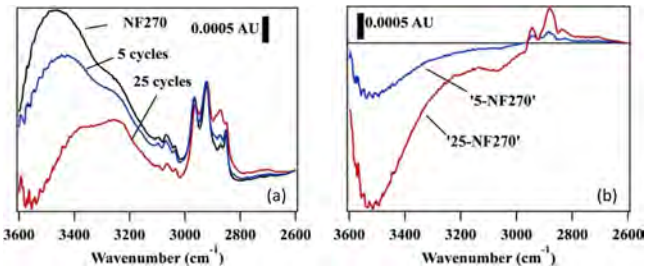

Figure 3. ATR−FTIR absorbance spectra for the hydrogen bond region of NF270 and EG-alucone coated NF270 membranes. (a) C−H, N−H, and hydrogen bond region spectra of NF270 (black trace), NF270 coated with 5 cycles (blue trace), and 25 cycles (red trace) of EG-alucone. (b) Difference FTIR spectra of NF270 coated with 5 cycles ("5-NF270"; blue trace) and 25 cycles ("25-NF270"; red trace) of EG-alucone from the NF270 spectrum. All spectra were recorded with the Ge ATR crystal at an incidence and collection angle of 60° and a resolution of 4 cm^{-1}. At least 256 scans were averaged in each spectrum. Bare ATR crystal was used as a background. The membranes were soaked in water for three days the FTIR measurement. The small peaks at 3400−3600 cm^{-1} are due to water vapor in the measurement path not completely subtracted.

assign to EG.[19,38,39] The increase in $-CH_2$ stretching band intensity after five MLD cycles are smaller in comparison to the intensity decrease of N−H peaks, which suggests that in the first five cycles, TMA reacts with functional groups of the active layer. In comparison, the large change in $-CH_2$ stretching bands after 25 MLD cycles (Figure 3a), indicates deposition of EG in or on the active layer, which is further supported by the increase in oxygen surface concentration found by XPS (see increased peak area in Figure S10c). Therefore, it seems that after 25 MLD cycles, the precursors of the MLD react with both the OH groups of EG and N−H groups of the piperazine. Further research of the exact reaction path, for example, by in situ FTIR, quartz crystal microbalance, and solid-state nuclear magnetic resonance spectroscopy (of ^{13}C, ^{2}H, ^{15}N, ^{18}O)[40] will be useful to pinpoint the stage at which the transition from reaction with active layer groups to EG groups take place.

In light of the above results, we suggest that there are three stages along the MLD process: stage 1 (<10 cycles)—nucleation by the reaction of TMA with the active layer functional groups, with minimal change of the morphology. Stage 2 (10−35 cycles)—Both EG-alucone deposition and transformation of the membrane active layer morphology occur and result in partial exposure of the supporting polysulfone threads. Stage 3 (>35 cycles)—coating of the modified surface and EG-alucone layer growth. As the EG-alucone layer becomes thicker its registration with the membrane texture (i.e., threads) weakens, and the elongated surface features become less prominent, irregular, and smaller. Our results are in agreement with previous work by Parsons and co-workers, who found that during ALD of Al_2O_3, TMA penetrates amide polymers and reacts with sub-surface functional groups.[41] Whereas for other materials and operating conditions (e.g., ALD of TiO_2 at ∼100 °C,[31,37]), uniform coating with no infiltration was reported. This points to the complexity of ALD/MLD on polymeric materials, which is a topic of ongoing research.[41−46] In this work, we observed significant changes in the morphology of the membrane active layer, which occurred at distinct MLD cycles along the deposition process and subsequently influenced the filtration

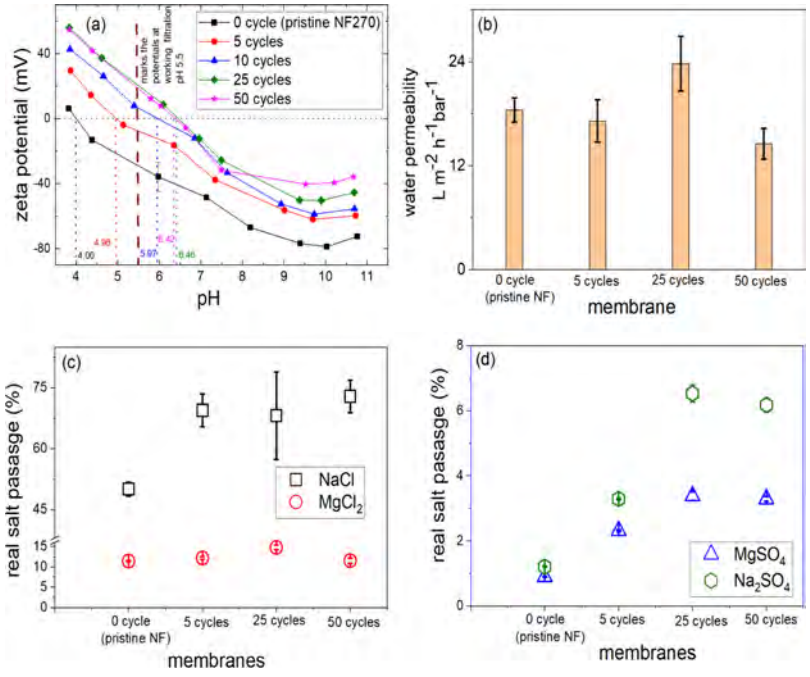

Figure 4. (a) Zeta potential of the membranes as a function of solution pH, (b) *water permeability* (at 4 bar), and the real salt passages (at 4 bar) for the (c) Cl^- based and (d) SO_4^{2-} based salts for membranes modified with varying MLD cycles. The marked numbers in the zeta potential plot are the IEPs. Post MLD modification, the membranes were soaked in water for 3 days before the zeta potential measurement at 23 °C (room temperature). The errors of zeta potential data are directly obtained from the analyzing instrument. In fig c and d, the salt concentration in feed solution—2 $g{\cdot}L^{-1}$, feed solution pH—5.5 ± 0.1, temperature—23 ± 1 °C, crossflow velocity—23 $cm{\cdot}s^{-1}$. The errors on *water permeability* are the standard deviations associated with three independent repetitions of each measurement using fresh membrane each time. The errors on the salt passages are the propagated ones obtained from the standard deviations of R_o.

https://dx.doi.org/10.1021/acsami.0c16569
ACS Appl. Mater. Interfaces 2020, 12, 53356−53364

performances of the membranes as described below in Section 3.4.

3.3. Hydrophilicity and Surface Charge. The zeta potential measurement (indicating surface charge) of NF270 is well-reported in the literature.[47] Based on the pKa values of the surface functional groups, at a pH < iso-electric point (IEP), the functional groups of the active layer are protonated (R-COOH and R-NH_3^+), while above the IEP, they are deprotonated (R-COO^- and R-NH_2). This explains the negative charge on the NF270 membrane at pH > 4.0. EG-alucone is converted to positively charged (IEP ~ 9[48]) alumina when soaked in water for ~3 days. Hence, the surface charge of the EG-alucone modified NF270 membrane becomes more positive and the corresponding IEP shifts toward higher values. The uncoated/unreacted functional groups of the NF270 active layer as well as the deposited EG-alucone both are expected to contribute toward the surface charge of the MLD modified membrane and hence, with increased MLD cycles, the membrane surface charge should be shifted to positive. Indeed, at the pH (5.5 ± 0.1) of the feed solution in the following filtration experiments, the zeta potential of pristine NF270 membrane gradually changed toward positive values with an increase in MLD cycles (Figure 4a). Interestingly, while the pristine membrane had an IEP of 4.0, in agreement with previous reports,[9,37] the IEP of the modified membranes gradually shifted with progressive MLD cycles until it reached ~6.4 after 25 MLD cycles (Figure 4a). The filtration results of different cations (as described and discussed in Section 3.4.2) although suggests a continuous increase in the membrane positive surface charge beyond 25 MLD cycles, but we did not observe any further corresponding increase in the IEP. Nevertheless, the higher zeta potential was measured at 50 cycles over 25 cycles at pH > IEP, supporting the addition of positive charge, which was not probed by the streaming potential measurement at lower pH. MLD of EG-alucone also resulted in lowering the membrane hydrophilicity, as the water contact angle for membranes subjected to five cycles of MLD was noticeably higher (~87°; Figure S12) than the contact angle of pristine membranes (~12°) or membranes subjected to 25 and 50 cycles (57−60°).

3.4. Filtration Performance. *3.4.1. Water Permeability and Stability.* The changes in the pure water permeability of the modified membranes correlate with the morphological changes described above (Figure 4b−d). After five cycles of MLD, the *water permeability* of the membrane (18.4 ± 1.4 L·m^{-2}·h^{-1}·bar^{-1}) was almost comparable to that of the pristine NF270 (17.2 ± 2.4 L·m^{-2}·h^{-1}·bar^{-1}). This indicated that the effective pore size and porosity remained mostly unchanged, which is in line with the negligible morphological change (Figure 2a,b) we observed. After 25 MLD cycles, a large increase in permeability was observed—33% with respect to pristine NF270. We attribute that to partial etching of the active polyamide-piperazine layer, thus introducing small defects (i.e., regions of higher water flux) that increased the water permeability. This result is in line with the morphological and chemical changes in the active layer we observed after 25 MLD cycles (see Sections 3.1 and 3.2). After 50 MLD cycles, the water permeability decreased by 21% in comparison to the unmodified NF270, probably because the active layer surface and the defects were coated by the EG-alucone layer. These changes are small compared to similar previous work[37] in which the permeability reduced by 90% after 50 ALD cycles of TiO_2. Notably, in this work, the EG-alucone treated membranes were stable in filtration experiments up to 24 h. Only a marginal drop in $MgSO_4$ rejection and *water permeability* (0.4 and 3%, respectively, Figure S15), and a small change in IEP (<0.5 pH units, Figure S13), were observed.

3.4.2. Passage of Single Salts and Associated Selectivities. Polymeric NF membranes such as the pristine NF270 are characterized by sub-nm scale effective pore size (0.5−2 nm),[34] and low dielectric constant in the pores[49,50] relative to unconfined water. These properties lead to the preferential passage of monovalent ions over bivalent ions because the strength of both steric and dielectric exclusion increases with the valence of ions regardless of their charge sign. From water softening perspective, steric and dielectric exclusion in NF270 overshadows electrostatic exclusion, meaning that even though the membrane is negatively charged at pH > 4 (Figure 4a), the passage of monovalent cations (e.g., Na^+) is still preferred over bivalent cations (e.g., Mg^{2+}). However, the fixed negative charge in NF270 dictated by the polyamide piperazine chemistry reduces the overall exclusion of bivalent cations and limits the selective rejection of Mg^{2+} over Na^+. Suppressing the membrane's negative charge while inflicting minimal damage to its water permeability is attainable using EG-alucone MLD, as reported herein. By measuring the trans-membrane transport of four different single salt solutions, we aimed at understanding how the amount of deposited EG-alucone (proportional to the number of MLD cycles), as well as the altered surface morphology, affect the interplay between the three main ion exclusion mechanisms. These relations are reflected in the selectivity; thereby understanding them would be beneficial for designing selective membranes in future work.

Changes in salt passage and selectivity in response to changes in the exclusion mechanism are already apparent in the NF270 membrane modified by five MLD cycles. The increase in the passage of the two symmetrical salts, NaCl and $MgSO_4$, indicates a decline in steric or dielectric exclusion, which are indifferent to ion charge sign. Because the water permeability after five MLD cycles did not change (Figure 4b), we conclude that the pore-size, and thus steric exclusion, also did not significantly change. Therefore, we propose that applying five MLD cycles decreases the dielectric exclusion of the membrane. Bivalent ions are affected more strongly from dielectric exclusion than monovalent ions,[51] therefore, the passage of $MgSO_4$ increased by a factor of ~2.5, while that of NaCl increased only by a factor of ~1.3 (Figure 4c,d), which is also reflected in the decrease in $\alpha_{MgSO_4}^{NaCl}$ (Figure 5d).

The salt passage and selectivity recorded after five MLD cycles were also affected by the change in electrostatic exclusion as a result of the change in the membrane's fixed charge (Figure 4a). Like dielectric exclusion, the electrostatic exclusion is stronger for multivalent ions, however only co-ions are excluded, while counter-ions undergo inclusion.[51] Therefore, the change in electrostatic exclusion is mostly reflected in the passage of the asymmetric salts. Accordingly, because of the suppression of negative fixed charge resulted from the MLD (Figure 4a), the greatest increase in the salt passage was observed for Na_2SO_4 due to a decrease in both electrostatic and dielectric exclusion. In contrast, the passage of $MgCl_2$ did not significantly change because, for this salt, the decrease in electrostatic exclusion counteracted the decrease in dielectric exclusion. This explanation is also supported by the increase in $\alpha_{MgCl_2}^{Na_2SO_4}$ by almost threefold which is the sharpest increase

https://dx.doi.org/10.1021/acsami.0c16569
ACS Appl. Mater. Interfaces 2020, 12, 53356−53364

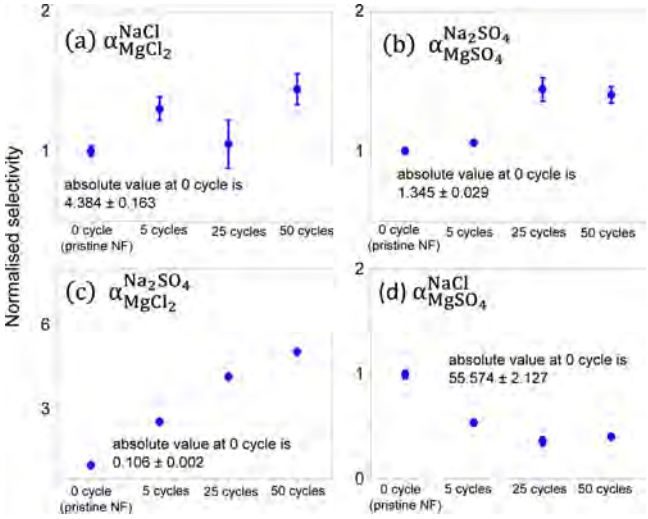

Figure 5. Normalised transport selectivity between (a) NaCl and $MgCl_2$, (b) Na_2SO_4 and $MgSO_4$, (c) Na_2SO_4 and $MgCl_2$, (d) NaCl and $MgSO_4$. The selectivity (α^i_j) factors have been calculated using eq 2 and then normalized by the selectivity of the pristine NF270 (0 cycle) membrane. Salt concentration in feed solution—2 g·L^{-1}, feed solution pH—5.5 ± 0.1, temperature—23 ± 1 °C, crossflow velocity—23 cm·s^{-1}, applied pressure—4 bar. The errors are the propagated ones obtained from the errors of observed rejections. For most of the experimental points, the error bars are of the size of the symbols.

among all of the recorded selectivities (Figure 5c). Similarly, $\alpha^{Na_2SO_4}_{MgSO_4}$ only slightly increased (Figure 5b) because of a balance between the dielectric exclusion (stronger for $MgSO_4$) to electrostatic exclusion (stronger for Na_2SO_4). A moderate increase in $\alpha^{NaCl}_{MgCl_2}$ suggests that both salts are influenced by the dielectric effect, yet the symmetric NaCl is less affected by the charge. Electrostatic exclusion thus plays a significant role in decreasing the passage of magnesium salts, demonstrating the importance of controlling the fixed charge for enhancing softening efficiency.

After subjecting the NF270 membranes to 25 MLD cycles, structural and chemical changes continue to affect the interplay between exclusion mechanisms, influencing the transport of ions. At 25 MLD cycles, defects in the active layer created regions of higher solvent flux, as indicated by the significant increase in water permeability. A decrease in steric exclusion for all ions is therefore expected, while a further decrease in dielectric exclusion cannot be ruled out. Because both these mechanisms exclude multivalent ions more strongly, $\alpha^{NaCl}_{MgSO_4}$ is further decreased compared to zero and five cycles (Figure 5d). Interestingly, the average NaCl passage did not significantly change for the number of MLD cycles >5, indicating that the steric exclusion of the monovalent ions was already low at 5 MLD.

In addition to the structural changes, applying 25 MLD cycles altered the surface charge from negative to positive at the working pH of 5.6 (Figure 4a), as reflected most clearly in the rapid increase of $\alpha^{Na_2SO_4}_{MgCl_2}$ (Figure 5c). The decrease in $\alpha^{NaCl}_{MgCl_2}$ (Figure 5a) is mainly due to a minor increase in $MgCl_2$ passage (Figure 4c), indicating that the decrease in steric exclusion had a stronger effect on Mg^{2+} permeability than the increase in electrostatic exclusion (this is not conclusive although because of the large experimental uncertainty at this stage). Na_2SO_4 passage increased most sharply when going from 5 to 25 MLD cycles, due to the decrease in both electrostatic and steric (possibly also dielectric) exclusion of SO_4^{2-} ions, which dominates Na_2SO_4 permeability. Because the passage of the symmetric $MgSO_4$ was not affected by electrostatic exclusion, $\alpha^{Na_2SO_4}_{MgSO_4}$ further, decrease at this stage (Figure 5b).

Going from 25 to 50 MLD cycles, the defects in the membrane were covered by a thicker nanoporous EG-alucone layer as indicated by the decrease in water permeability (Figure 4b). This is supported by the decrease in the salt passage for the three salts containing divalent ions, which are more prone to steric exclusion than NaCl. Although the change of zeta-potential (Figure 4a) was insignificant between 25 and 50 MLD cycles, the role of electrostatic exclusion in determining ion selectivities is apparent in the further increase of $\alpha^{Na_2SO_4}_{MgCl_2}$ (Figure 5c). Because zeta-potential only captures the surface charge, we attribute this effect to the penetration of EG-alucone into the exposed defects. The increase in $\alpha^{NaCl}_{MgCl_2}$ and a decrease in $\alpha^{Na_2SO_4}_{MgSO_4}$ further supports the conjecture of positive charge accumulation in the subsurface (Figure 5a,b).

Overall, the change in the experimental salt passage and selectivity values for the tested modified membranes was correlated to the chemical/morphological changes. This correlation is plausibly explained through known exclusion mechanisms, demonstrating the potential to rationally tune the ion-selectivity of NF using MLD of EG-alucone.

3.4.3. Ion Rejection from Brackish Water and Associated Transport Selectivity. The overall increase in the selectivity of sodium over magnesium salts, induced by the MLD process, points at the potential to improve water softening. However, practical water softening involves NF of mixed ion solutions, which is different from the single salts' behavior and harder to predict because of the interdependency of all ion fluxes through electromigration and the complex influence of ion concentrations on ions permeance.[52] We, therefore, tested the functionality of EG-alucone coated membranes (50 MLD cycles) using *real brackish water* (4 bar, ion concentration is given in Table S4) and compared its performances to those of pristine NF270 membranes (0 cycles; Table 1).

For the brackish water we used, the rejection of Na^+ was low (11−13%) with no significant difference between the coated and pristine membranes, while the rejection of both Mg^{2+} and Ca^{2+} increased (by 6.3 and 10.4%, respectively). Accordingly, the permselectivity of Na^+ over these bivalent cations increased. The improved selectivity was due to the modification of membrane charge, as was also indicated by the decrease in SO_4^{2-} rejection. In terms of hardness, this *brackish water* falls under the category of "very hard" (>180 mg/L as $CaCO_3$) water with a hardness value of 619 mg·L^{-1} as $CaCO_3$. The permeate produced by the pristine membrane was still considered "very hard", with an average hardness of 223 mg·L^{-1} as $CaCO_3$, whereas the permeate produced by the coated membrane had an average hardness of 165 mg·L^{-1} as $CaCO_3$, which is in the category "hard". This results thus highlight the applicability of the modified membranes in real environments for hardness removal, that is, *water softening*, which is a step forward beyond recent ALD/MLD work,[31−33,37] which only examined synthetic single salt solutions. A comparison to previous works[9,10,14,31−33,37,53−58]

https://dx.doi.org/10.1021/acsami.0c16569
ACS Appl. Mater. Interfaces 2020, 12, 53356−53364

Table 1. Ion Rejection and Associated Transport Selectivities of Na^+ Over Different Cations (K^+, Mg^{2+}, and Ca^{2+}), as Obtained from the Filtration of *Real Brackish Water*

membrane		0 cycles (pristine NF270)	50 cycles
observed rejections (R_o)	Na^+	11.6 ± 0.6	12.1 ± 1.9
	K^+	17.9 ± 1.6	33.8 ± 2.2
	Mg^{2+}	75.1 ± 1.2	81.4 ± 1.9
	Ca^{2+}	55.1 ± 1.5	65.5 ± 3.3
	SO_4^{2-}	96.8 ± 0.9	95.7 ± 0.7
selectivity of Na^+ over	K^+	1.1 ± 0.1	1.3 ± 0.1
	Mg^{2+}	3.6 ± 0.2	4.8 ± 0.5
	Ca^{2+}	1.90 ± 0.02	2.8 ± 0.2

Ion selectivities calculated using the observed rejections (R_0) in eq 2. *Brackish water* ionic composition is in Table S4, feed solution pH—5.8, temperature—23 ± 1 °C, crossflow velocity—23 $cm \cdot s^{-1}$, applied pressure—4 bar. The errors are the standard deviations associated with four independent repetitions of each measurement.

on selective NF membranes (see Table S5) shows that none of these membranes have selectivity and water permeability that are both higher than the membrane coated with EG-alucone (50 MLD cycles). Although this comparison should be with caution (because selectivity can be affected by the experimental conditions) it suggests that MLD coating applied to thin-film composite NF can further mitigate the selectivity−permeability trade-off.

4. CONCLUSIONS

In this work, we used a low-temperature MLD procedure for modifying and coating a thin film composite NF membrane with a layer of positively-charged EG-alucone. Using this method, we were able to tune the ion-selectivity of the membranes by controlling the amount of EG-alucone deposited. Unlike the similar previous work,[33−35,38] the coating did not significantly damage the water permeability of the membrane, and the coating was stable in a long filtration process. We related the change in ion-selectivities, as measured from single salts filtration experiments, to the morphological and chemical changes in the membrane affected by the EG-alucone and interpreted the trends according to known ion exclusion mechanisms. When tested using real brackish groundwater, the coated membrane was found to have improved efficiency of water softening compared to the uncoated membrane. Because a variety of precursors are available in MLD, this work opens a path for developing different coatings and procedures for expanding ion-selectivity of thin-film composite NF membranes beyond the limitations of the base polymer chemistry.

■ ASSOCIATED CONTENT

Supporting Information

The Supporting Information is available free of charge at https://pubs.acs.org/doi/10.1021/acsami.0c16569.

Detailed description of all material characterizations, figures for MLD and filtration setup, tabulated observed and real salt rejections, mass transfer coefficients, ion-selectivities, and *brackish water* composition (PDF)

■ AUTHOR INFORMATION

Corresponding Authors

Eran Edri − *Department of Chemical Engineering, Ben-Gurion University of the Negev, Beer-Sheva 8410501, Israel;* orcid.org/0000-0003-4593-6489; Email: edrier@bgu.ac.il

Oded Nir − *Blaustein Institutes for Desert Research, Zuckerberg Institute for Water Research, Ben-Gurion University of the Negev, Beer-Sheva 8499000, Israel;* orcid.org/0000-0003-2061-9188; Email: odni@bgu.ac.il

Authors

Sanhita Chaudhury − *Blaustein Institutes for Desert Research, Zuckerberg Institute for Water Research, Ben-Gurion University of the Negev, Beer-Sheva 8499000, Israel;* orcid.org/0000-0001-5874-5855

Eyal Wormser − *Department of Chemical Engineering, Ben-Gurion University of the Negev, Beer-Sheva 8410501, Israel*

Yuval Harari − *Department of Chemical Engineering, Ben-Gurion University of the Negev, Beer-Sheva 8410501, Israel*

Complete contact information is available at: https://pubs.acs.org/10.1021/acsami.0c16569

Notes

The authors declare no competing financial interest.

■ ACKNOWLEDGMENTS

S.C. is highly grateful to the Marcus family donation to the Water Science Fund of the Ben-Gurion University of the Negev for her postdoctoral scholarship.

■ REFERENCES

(1) Guo, S.; Chen, X.; Wan, Y.; Feng, S.; Luo, J. Custom-Tailoring Loose Nanofiltration Membrane for Precise Biomolecule Fractionation: New Insight into Post-Treatment Mechanisms. *ACS Appl. Mater. Interfaces* **2020**, *12*, 13327−13337.

(2) López, J.; Reig, M.; Gibert, O.; Cortina, J. L. Increasing Sustainability on the Metallurgical Industry by Integration of Membrane Nanofiltration Processes: Acid Recovery. *Sep. Purif. Technol.* **2019**, *226*, 267−277.

(3) Nir, O.; Sengpiel, R.; Wessling, M. Closing the Cycle: Phosphorus Removal and Recovery from Diluted Effluents Using Acid Resistive Membranes. *Chem. Eng. J.* **2018**, *346*, 640−648.

(4) Luo, J.; Wan, Y. Effects of pH and Salt on Nanofiltration—a Critical Review. *J. Membr. Sci.* **2013**, *438*, 18−28.

(5) Water Softener Market Size to Exceed $10 Billion by 2024: Global Market Insights, Inc. August, 2020, https://www.prnewswire.com/news-releases/water-softener-market-size-to-exceed-10-billion-by-2024-global-market-insights-inc--821852784.html. (accessed on 12th November, 2020).

(6) Seo, S.-J.; Jeon, H.; Lee, J. K.; Kim, G.-Y.; Park, D.; Nojima, H.; Lee, J.; Moon, S.-H. Investigation on Removal of Hardness Ions by Capacitive Deionization (CDI) for Water Softening Applications. *Water Res.* **2010**, *44*, 2267−2275.

(7) Fridman-Bishop, N.; Nir, O.; Lahav, O.; Freger, V. Predicting the Rejection of Major Seawater Ions by Spiral-Wound Nanofiltration Membranes. *Environ. Sci. Technol.* **2015**, *49*, 8631−8638.

(8) Zhang, H.; He, Q.; Luo, J.; Wan, Y.; Darling, S. B. Sharpening Nanofiltration: Strategies for Enhanced Membrane Selectivity. *ACS Appl. Mater. Interfaces* **2020**, *12*, 39948−39966.

(9) Ng, L. Y.; Mohammad, A. W.; Ng, C. Y.; Leo, C. P.; Rohani, R. Development of Nanofiltration Membrane with High Salt Selectivity and Performance Stability Using Polyelectrolyte Multilayers. *Desalination* **2014**, *351*, 19−26.

(10) Ouyang, L.; Malaisamy, R.; Bruening, M. L. Multilayer Polyelectrolyte Films as Nanofiltration Membranes for Separating Monovalent aseelctive removal of divalentnd Divalent Cations. *J. Membr. Sci.* **2008**, *310*, 76−84.
(11) Cheng, W.; Liu, C.; Tong, T.; Epsztein, R.; Sun, M.; Verduzco, R.; Ma, J.; Elimelech, M. Selective Removal of Divalent Cations by Polyelectrolyte Multilayer Nanofiltration Membrane: Role of Polyelectrolyte Charge, Ion Size, and Ionic Strength. *J. Membr. Sci.* **2018**, *559*, 98−106.
(12) DuChanois, R. M.; Epsztein, R.; Trivedi, J. A.; Elimelech, M. Controlling Pore Structure of Polyelectrolyte Multilayer Nanofiltration Membranes by Tuning Polyelectrolyte-Salt Interactions. *J. Membr. Sci.* **2019**, *581*, 413−420.
(13) Hu, R.; He, Y.; Zhang, C.; Zhang, R.; Li, J.; Zhu, H. Graphene Oxide-Embedded Polyamide Nanofiltration Membranes for Selective Ion Separation. *J. Mater. Chem. A* **2017**, *5*, 25632−25640.
(14) Gao, S.; Zhu, Y.; Gong, Y.; Wang, Z.; Fang, W.; Jin, J. Ultrathin Polyamide Nanofiltration Membrane Fabricated on Brush-Painted Single-Walled Carbon Nanotube Network Support for Ion Sieving. *ACS Nano* **2019**, *13*, 5278−5290.
(15) Sadeghi, I.; Kronenberg, J.; Asatekin, A. Selective Transport through Membranes with Charged Nanochannels Formed by Scalable Self-Assembly of Random Copolymer Micelles. *ACS Nano* **2018**, *12*, 95−108.
(16) Geise, G. M.; Park, H. B.; Sagle, A. C.; Freeman, B. D.; McGrath, J. E. Water Permeability and Water/Salt Selectivity Tradeoff in Polymers for Desalination. *J. Membr. Sci.* **2011**, *369*, 130−138.
(17) Zhang, R.; Tian, J.; Gao, S.; Van der Bruggen, B. How to Coordinate the Trade-Off Between Water Permeability and Salt Rejection in Nanofiltration? *J. Mater. Chem. A* **2020**, *8*, 8831−8847.
(18) Kumar, M.; Khan, M. A.; Arafat, H. A. Recent Developments in the Rational Fabrication of Thin Film Nanocomposite Membranes for Water Purification and Desalination. *ACS Omega* **2020**, *5*, 3792−3800.
(19) Dameron, A. A.; Seghete, D.; Burton, B. B.; Davidson, S. D.; Cavanagh, A. S.; Bertrand, J. A.; George, S. M. Molecular Layer Deposition of Alucone Polymer Films Using Trimethylaluminum and Ethylene Glycol. *Chem. Mater.* **2008**, *20*, 3315−3326.
(20) George, S. M.; Yoon, B.; Dameron, A. A. Surface Chemistry for Molecular Layer Deposition of Organic and Hybrid Organic−Inorganic Polymers. *Acc. Chem. Res.* **2009**, *42*, 498−508.
(21) Wu, S.-L.; Liu, F.; Yang, H.-C.; Darling, S. B. Recent Progress in Molecular Engineering to Tailor Organic−Inorganic Interfaces in Composite Membranes. *Mol. Syst. Des. Eng.* **2020**, *5*, 433−444.
(22) Choi, D.-w.; Yoo, M.; Lee, H. M.; Park, J.; Kim, H. Y.; Park, J.-S. A Study on the Growth Behavior and Stability of Molecular Layer Deposited Alucone Films Using Diethylene Glycol and Trimethyl Aluminum Precursors, and the Enhancement of Diffusion Barrier Properties by Atomic Layer Deposited Al_2O_3 Capping. *ACS Appl. Mater. Interfaces* **2016**, *8*, 12263−12271.
(23) Yang, H.-C.; Waldman, R. Z.; Chen, Z.; Darling, S. B. Atomic Layer Deposition for Membrane Interface Engineering. *Nanoscale* **2018**, *10*, 20505−20513.
(24) Meng, X. An Overview of Molecular Layer Deposition for Organic and Organic−Inorganic Hybrid Materials: Mechanisms, Growth Characteristics, and Promising Applications. *J. Mater. Chem. A* **2017**, *5*, 18326−18378.
(25) Dorsey, K. J.; Pearson, T. G.; Esposito, E.; Russell, S.; Bircan, B.; Han, Y.; Miskin, M. Z.; Muller, D. A.; Cohen, I.; McEuen, P. L. Atomic Layer Deposition for Membranes, Metamaterials, and Mechanisms. *Adv. Mater.* **2019**, *31*, 1901944.
(26) Wa, Q.; Xiong, W.; Zhao, R.; He, Z.; Chen, Y.; Wang, X. Nanoscale $Ni(OH)_x$ Films on Carbon Cloth Prepared by Atomic Layer Deposition and Electrochemical Activation for Glucose Sensing. *ACS Appl. Nano Mater.* **2019**, *2*, 4427−4434.
(27) Weber, M.; Koonkaew, B.; Balme, S.; Utke, I.; Picaud, F.; Iatsunskyi, I.; Coy, E.; Miele, P.; Bechelany, M. Boron Nitride Nanoporous Membranes with High Surface Charge by Atomic Layer Deposition. *ACS Appl. Mater. Interfaces* **2017**, *9*, 16669−16678.
(28) Lee, B. H.; Yoon, B.; Anderson, V. R.; George, S. M. Alucone Alloys with Tunable Properties Using Alucone Molecular Layer Deposition and Al_2O_3 Atomic Layer Deposition. *J. Phys. Chem. C* **2012**, *116*, 3250−3257.
(29) Jen, S.-H.; George, S. M.; McLean, R. S.; Carcia, P. F. Alucone Interlayers to Minimize Stress Caused by Thermal Expansion Mismatch Between Al_2O_3 Films and Teflon Substrates. *ACS Appl. Mater. Interfaces* **2013**, *5*, 1165−1173.
(30) Van de Kerckhove, K.; Barr, M. K. S.; Santinacci, L.; Vereecken, P. M.; Dendooven, J.; Detavernier, C. The Transformation Behaviour of "Alucones", Deposited by Molecular Layer Deposition, in Nanoporous Al_2O_3 Layers. *Dalton Trans.* **2018**, *47*, 5860−5870.
(31) Chen, H.; Jia, X.; Wei, M.; Wang, Y. Ceramic Tubular Nanofiltration Membranes with Tunable Performances by Atomic Layer Deposition and Calcination. *J. Membr. Sci.* **2017**, *528*, 95−102.
(32) Song, Z.; Fathizadeh, M.; Huang, Y.; Chu, K. H.; Yoon, Y.; Wang, L.; Xu, W. L.; Yu, M. TiO_2 Nanofiltration Membranes Prepared by Molecular Layer Deposition for Water Purification. *J. Membr. Sci.* **2016**, *510*, 72−78.
(33) Wu, S.; Wang, Z.; Xiong, S.; Wang, Y. Tailoring TiO_2 Membranes for Nanofiltration and Tight Ultrafiltration by Leveraging Molecular Layer Deposition and Crystallization. *J. Membr. Sci.* **2019**, *578*, 149−155.
(34) Zhang, H.; Quan, X.; Chen, S.; Fan, X.; Wei, G.; Yu, H. Combined Effects of Surface Charge and Pore Size on Co-Enhanced Permeability and Ion Selectivity through RGO-OCNT Nanofiltration Membranes. *Environ. Sci. Technol.* **2018**, *52*, 4827−4834.
(35) Yao, Z.; Guo, H.; Yang, Z.; Qing, W.; Tang, C. Y. Preparation of Nanocavity-Contained Thin Film Composite Nanofiltration Membranes with Enhanced Permeability and Divalent to Monovalent Ion Selectivity. *Desalination* **2018**, *445*, 115−122.
(36) Boo, C.; Wang, Y.; Zucker, I.; Choo, Y.; Osuji, C. O.; Elimelech, M. High Performance Nanofiltration Membrane for Effective Removal of Perfluoroalkyl Substances at High Water Recovery. *Environ. Sci. Technol.* **2018**, *52*, 7279−7288.
(37) Zhou, X.; Zhao, Y.-Y.; Kim, S.-R.; Elimelech, M.; Hu, S.; Kim, J.-H. Controlled TiO_2 Growth on Reverse Osmosis and Nanofiltration Membranes by Atomic Layer Deposition: Mechanisms and Potential Applications. *Environ. Sci. Technol.* **2018**, *52*, 14311−14320.
(38) Groner, M. D.; Fabreguette, F. H.; Elam, J. W.; George, S. M. Low-temperature Al_2O_3 Atomic Layer Deposition. *Chem. Mater.* **2004**, *16*, 639−645.
(39) Van de Kerckhove, K.; Barr, M. K. S.; Santinacci, L.; Vereecken, P. M.; Dendooven, J.; Detavernier, C. The Transformation Behaviour of "Alucones", Deposited by Molecular Layer Deposition, in Nanoporous Al_2O_3 Layers. *Dalton Trans.* **2018**, *47*, 5860−5870.
(40) Duan, P.; Moreton, J. C.; Tavares, S. R.; Semino, R.; Maurin, G.; Cohen, S. M.; Schmidt-Rohr, K. Polymer Infiltration into Metal−Organic Frameworks in Mixed-Matrix Membranes Detected in Situ by NMR. *J. Am. Chem. Soc.* **2019**, *141*, 7589−7595.
(41) Spagnola, J. C.; Gong, B.; Arvidson, S. A.; Jur, J. S.; Khan, S. A.; Parsons, G. N. Surface and Sub-Surface Reactions During Low Temperature Aluminium Oxide Atomic Layer Deposition on Fiber-Forming Polymers. *J. Mater. Chem.* **2010**, *20*, 4213−4222.
(42) Waldman, R. Z.; Mandia, D. J.; Yanguas-Gil, A.; Martinson, A. B. F.; Elam, J. W.; Darling, S. B. The Chemical Physics of Sequential Infiltration Synthesis—A Thermodynamic and Kinetic Perspective. *J. Chem. Phys.* **2019**, *151*, 190901.
(43) Waldman, R. Z.; Yang, H.-C.; Mandia, D. J.; Nealey, P. F.; Elam, J. W.; Darling, S. B. Janus Membranes via Diffusion-Controlled Atomic Layer Deposition. *Adv. Mater. Interfaces* **2018**, *5*, 1800658.
(44) Obuchovsky, S.; Frankenstein, H.; Vinokur, J.; Hailey, A. K.; Loo, Y.-L.; Frey, G. L. Mechanism of Metal Oxide Deposition from Atomic Layer Deposition Inside Nonreactive Polymer Matrices: Effects of Polymer Crystallinity and Temperature. *Chem. Mater.* **2016**, *28*, 2668−2676.

https://dx.doi.org/10.1021/acsami.0c16569
ACS Appl. Mater. Interfaces 2020, 12, 53356−53364

(45) Weisbord, I.; Shomrat, N.; Azoulay, R.; Kaushansky, A.; Segal-Peretz, T. Understanding and Controlling Polymer-Organometallic Precursor Interactions in Sequential Infiltration Synthesis. *Chem. Mater.* **2020**, *32*, 4499−4508.
(46) Leng, C. Z.; Losego, M. D. Vapor Phase Infiltration (VPI) for Transforming Polymers into Organic−Inorganic Hybrid Materials: A Critical Review of Current Progress and Future Challenges. *Mater. Horiz.* **2017**, *4*, 747−771.
(47) Ortiz-Albo, P.; Ibañez, R.; Urtiaga, A.; Ortiz, I. Phenomenological Prediction of Desalination Brines Nanofiltration Through the Indirect Determination of Zeta Potential. *Sep. Purif. Technol.* **2019**, *210*, 746−753.
(48) Singh, B. P.; Menchavez, R.; Takai, C.; Fuji, M.; Takahashi, M. Stability of Dispersions of Colloidal Alumina Particles in Aqueous Suspensions. *J. Colloid Interface Sci.* **2005**, *291*, 181−186.
(49) Micari, M.; Diamantidou, D.; Heijman, B.; Moser, M.; Haidari, A.; Spanjers, H.; Bertsch, V. Experimental and Theoretical Characterization of Commercial Nanofiltration Membranes for the Treatment of Ion Exchange Spent Regenerant. *J. Membr. Sci.* **2020**, *606*, 118117.
(50) Zhao, K.; Lu, Q.; Su, W. Estimation of Electrical Parameters Inside Nanofiltration Membranes in Various Electrolyte Solutions by Dielectric Spectroscopy Analysis. *RSC Adv.* **2014**, *4*, 63085−63099.
(51) Yaroshchuk, A.; Bruening, M. L.; Zholkovskiy, E. Modelling Nanofiltration of Electrolyte Solutions. *Adv. Colloid Interface Sci.* **2019**, *268*, 39−63.
(52) Freger, V. Ion Partitioning and Permeation in Charged Low-T* Membranes. *Adv. Colloid Interface Sci.* **2020**, *277*, 102107.
(53) Hu, R.; He, Y.; Zhang, C.; Zhang, R.; Li, J.; Zhu, H. Graphene Oxide-Embedded Polyamide Nanofiltration Membranes for Selective Ion Separation. *J. Mater. Chem. A* **2017**, *5*, 25632−25640.
(54) Nativ, P.; Lahav, O.; Gendel, Y. Separation of Divalent and Monovalent Ions Using Flow-Electrode Capacitive Deionization with Nanofiltration Membranes. *Desalination* **2018**, *425*, 123−129.
(55) Li, Y.; Wong, E.; Mai, Z.; Van der Bruggen, B. Fabrication of Composite Polyamide/Kevlar Aramid Nanofiber Nanofiltration Membranes with High Permselectivity in Water Desalination. *J. Membr. Sci.* **2019**, *592*, 117396.
(56) Liu, C.; Shi, L.; Wang, R. Crosslinked Layer-by-Layer Polyelectrolyte Nanofiltration Hollow Fiber Membrane for Low-Pressure Water Softening with the Presence of SO_4^{2-} in Feed Water. *J. Membr. Sci.* **2015**, *486*, 169−176.
(57) Homayoonfal, M.; Akbari, A.; Mehrnia, M. R. Preparation of Polysulfone Nanofiltration Membranes by UV-Assisted Grafting Polymerization for Water Softening. *Desalination* **2010**, *263*, 217−225.
(58) Wang, J.; Wang, Z.; Liu, Y.; Wang, J.; Wang, S. Surface Modification of NF Membrane with Zwitterionic Polymer to Improve Anti-Biofouling Property. *J. Membr. Sci.* **2016**, *514*, 407−417.

https://dx.doi.org/10.1021/acsami.0c16569
ACS Appl. Mater. Interfaces 2020, 12, 53356−53364